Research Article

Microwave Emission and Scattering from Ocean Surface Waves in the Southern Beaufort Sea

Mukesh Gupta, Randall K. Scharien, and David G. Barber

Department of Environment and Geography, Wallace Building, Centre for Earth Observation Science,
Clayton H. Riddell Faculty of Environment, Earth, and Resources, University of Manitoba, Winnipeg, MB, Canada

Correspondence should be addressed to Mukesh Gupta; guptm@yahoo.com

Estimates of the relationships between geophysical variables and microwave backscatter/emission are important for the evaluation of atmosphere-ocean interaction, as well as energy, and mass transfer across this interface. We evaluate ship-based passive microwave brightness temperatures (T_b) at 37 and 89 GHz and active polarimetric backscatter at 5.5 GHz (C-band), as these relate to buoy-derived ocean wave parameters for distinct wave regimes in the southern Beaufort Sea. Microwave emission and backscatter are shown to be sensitive to the ocean surface physical roughness as defined by the significant wave height (H_{m0}), compared to wind speed. The T_b shows significant correlation with H_{m0}, with the strongest correlation for the H-polarization channel at 37 and 89 GHz. Active co-(γ_{co}) and cross-(γ_{cross}) polarization ratios at 40° incidence angle are associated with H_{m0}, with the γ_{co} increase proportional to H_{m0}. The polarimetric coherence parameter ρ_{VVHH} at 20° also shows an inverse relationship with H_{m0} because of an expected decorrelation of complex returns with greater surface roughness.

1. Introduction

The southern Beaufort Sea is of interest because of its dynamic seasonal ocean-sea ice-atmosphere interaction [1, 2] and the seasonal formation of flaw leads and polynyas [3, 4]. Microwave remote sensing has played a key role in investigations, with scientists studying the passive and active microwave signatures from the ocean surface for several decades. It has now been possible to estimate numerous geophysical parameters with sufficient accuracy based on microwave data collected using satellite sensors. However, relationship between surface waves and the radiative transfer across the atmosphere-ocean (AO) interface is, yet, not fully realized in the literature.

Ocean surface waves modify AO interaction and concurrently affect observed passive microwave brightness temperatures (T_b) and radar returns (hereinafter backscatter). Enhanced surface roughness from wind-generated surface waves significantly affects the formation and evolution of the oceanic boundary layer [5], which in turn causes greater atmospheric instability and turbulent exchange at the AO interface [6]. Physical roughness also acts as an important component of feedback processes which transfer heat and momentum across AO interface. Though there is good understanding of the transfer of wind energy to the ocean surface waves (aerodynamic roughness), the microwave behavior of related geophysical variables such as significant wave height (H_{m0}) (hereinafter wave height), power spectral density (PSD), ocean surface temperature, and near-surface water vapor is the subject of further study. Open water backscatter and T_b observations represent composite signals that contain contributions from the full suite of these variables. In accordance, the application of electromagnetic (EM) signatures to geophysical inversion algorithms first demands consideration of the full suite of variables.

Previous research into AO surface roughness from both passive and active microwave remote sensing indicates considerable gaps in understanding the EM response to roughness elements (e.g., whitecaps, sea spray, and wave RMS (root mean square) height and correlation length). Polarimetric passive microwave signatures of the ocean surface at frequencies 10.7, 19.35, and 37 GHz are well modeled by a two-scale polarimetric emission model [7, 8]; however, the assimilation of effects of wind direction, wind-generated waves, atmospheric stability, and sea foam into polarimetric emission models of ocean surface is a topic requiring further research.

The undulations of the ocean surface significantly affect the observed, frequency-dependent, T_b, which is dependent on the wind-induced wave structure, that is, the sea state and foam coverage [9, 10]. Kravtsov and Churyumov [11] mathematically delineated the effect of steep irregularities and wave slope on the T_b. Monahan and O'Muircheartaigh [12] used remote sensing to include whitecaps and foam in the wind retrieval algorithms. Wave height can also be linked to T_b as a close function of surface wind speed [13]. Nordberg et al. [14] provided the measurements of microwave emission at 19 GHz from a foam-covered and wind-driven sea. One observes an increase in the T_b with an increase in foam coverage and whitecaps in all surface conditions mentioned above.

Microwave C-band (5.5 GHz, 5.6 cm wavelength) backscatter is more reliable for studying ocean surface waves than shorter wavelength Ku-, Ka-, and X-bands. Capillarity and molecular viscosity (water temperature) strongly influence the radar return in these bands [15, 16]. There are numerous studies readily found on relationships between C-band copolarization backscatter (HH and VV) and wind speed and direction, with geophysical model transfer functions (e.g., CMOD) widely used to retrieve wind information from backscatter [17–20]. A power-law relationship holds for backscatter and friction velocity [21] and between backscatter and wind speed [22]. Keller et al. [22] also observed backscatter increasing with decreasing AO temperature difference. Thompson et al. [23] found that the observed copolarization ratio (HH/VV) is larger than predicted by backscatter models, as these models inadequately address the nonlinearity of the long-wave portion of a rough ocean surface. Thompson et al. [23] provided an incidence-angle-dependent polarization ratio model. Mouche et al. [24] extended this model to include wind speed, wind direction, sea state, and swell effects. The results of Mouche et al. [24] show that the copolarization ratio (γ_{co}) is dependent more on wave steepness than on wave height and wind speed.

The waves under rough conditions are typically 3–10 times larger than the incident radar wavelength at C-band [25, 26]. Kudryavtsev et al. [25] suggested a composite backscatter model for describing backscatter (at moderate incidence angles 20°–60°) from ocean surface waves which included non-Bragg scattering components caused by breaking waves (wavelength from few millimeters to few meters) based on wave breaking statistics proposed by Phillips [27]. One can use the γ_{co} to study the discrepancy between the Bragg model and observations, and it can explain the non-Bragg component of scattering [25]. Valenzuela [28] provided a review of the theories addressing EM wave interaction with the small gravity-capillary waves, citing Bragg (resonant) scattering as the most important mechanism of ocean surface—EM interaction. Energy dissipation over different length scales and breaking wave mechanisms is largely linked to non-Bragg scattering, though there is little understanding of their effects on backscatter. The H_{m0} and wave PSD measured from Waverider buoy are investigated here, which contain contributions from the non-Bragg scattering elements, using the cross-polarization channel ratio (γ_{cross}) and polarimetric coherence parameters, in addition to γ_{co}.
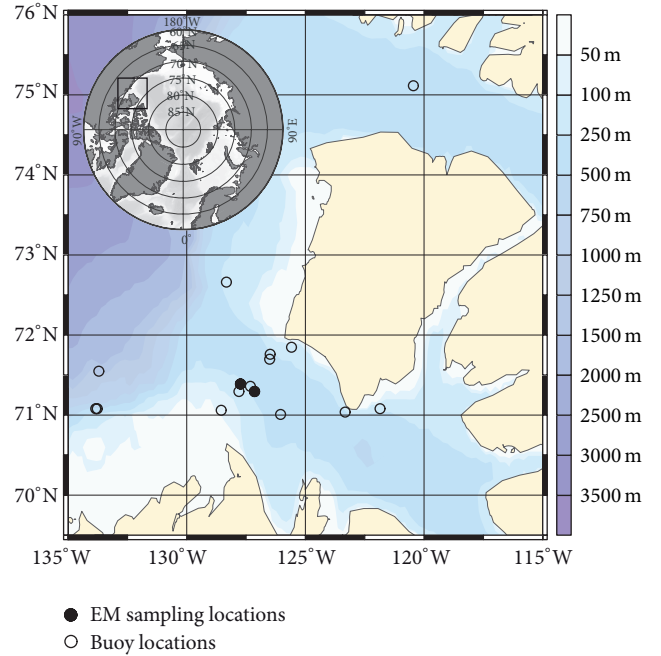

● EM sampling locations
○ Buoy locations

FIGURE 1: Study area showing DWR-G4 buoy and EM sampling locations.

This paper addresses open ocean surface waves (physical roughness) during the ice-free season, with the overarching objective, to further our understanding of the role of T_b and backscatter in estimating ocean surface waves and, by proxy, AO exchanges. We examine near surface (ship-based) passive microwave T_b (37 and 89 GHz) and polarimetric C-band backscatter, as these relate to buoy measurements of H_{m0} and PSD. This comparison is rarely available in the literature. We investigate the utility of γ_{co} and γ_{cross}, as well as polarimetric coherences from the ocean surface, to contribute to the realization of polarimetric synthetic aperture radar for deriving ocean surface wave information.

2. Materials and Methods

2.1. Study Area. The study area lies in Amundsen Gulf in the southern Beaufort Sea (Figure 1). The Cape Bathurst Polynya forms in the area and hosts several flaw leads throughout the winter [1] and the region becomes ice-free in the summer. We acquired field data between July 1 and 28, 2008 under the auspices of the Circumpolar Flaw Lead (CFL) System Study, an International Polar Year (IPY) project that took place between October 2007 and August 2008 aboard the Canadian Research Icebreaker *Amundsen* [29].

2.2. Instruments' Description and Data Collection. We acquired ocean wave height, wave steepness, wave period, and wave phase speed using a meteorological ocean (Datawell, Haarlem, The Netherlands) Mini Directional Waverider G4 (DWR-G4) buoy. The buoy has a hull diameter of 0.4 m and weight in air of 17 kg. The buoy is capable of measuring wave height and direction for periods of

TABLE 1: Technical properties and specifications of C-band scatterometer used.

System parameter	Value
RF output	5.25–5.75 GHz
Antenna diameter	0.61 m
Transmit bandwidth	5–500 MHz, user adjustable
Range resolution	0.3–30.0 meters, user adjustable
Antenna beamwidth	H-pol: 5.2° azimuth, 5.5° elevation V-pol: 5.6° azimuth, 5.3° elevation
Antenna gain	28 dB, nominal
Cross-polarization isolation	>30 dB, measured at the peak of the beam
Transmit/receive polarizations	Linear, vertical, and horizontal
Sensitivity, minimum NRCS at 15 m range	$-40 \, \text{dB} \, \text{m}^2/\text{m}^2$
Chirp length	Variable, 0.1–15.0 ms

Note. NRCS: normalized radar cross-section; RF: radio frequency.

1.6–100 sec and covers the expected range of wave periods observed in the Arctic (~60 sec; see, e.g., [30]). Wave height accuracy is 1 cm in all directions while freely floating. We computed H_{m0} from the zeroth moment of the wave spectrum. The accuracy of wave PSD, wavelength, and other derived wave parameters relies on wave height accuracy. We deployed the buoy by small boat at a minimum distance of 200 m to avoid interference by the *Amundsen*. Wave data were logged at 30-minute intervals from a stabilized accelerometer. We collected continuous meteorological data at one-minute interval from a tower mounted on the bow of the *Amundsen*. An RM-Young model 5103 Wind Monitor provided the wind speed (U) data at 14 m above sea level (ASL) at accuracy of ±0.3 m/s or 1% of the reading. The *Amundsen's* AXYS Automated Voluntary Observing Ship (AVOS) sensors provided water temperature at the sea surface with a resolution of 0.1°C and an accuracy of ±0.3°C.

We have used ship-based dual-polarized (H and V) passive microwave (Radiometrics, Boulder, CO, USA) radiometers operating at 37 and 89 GHz frequencies to acquire emissions at a fixed incidence angle of 53°, the same angle as the spaceborne SSM/I (Special Sensor Microwave/Imager) sensor and within 2° of the spaceborne AMSR-E (Advanced Microwave Scanning Radiometer—Earth Observing System) sensor. We installed the system on the rail mount on the port side of the *Amundsen* at approximately 12 m ASL. To convert recorded voltages to T_b, we followed the calibration method described by Farmer et al. [31]. The T_b data were acquired for 24-hour full cycle for all days and were averaged for every 30 minutes for the specified dates during the month of July 2008 at the locations shown in Figure 1. T_b data were matched with buoy data over 2–7 hours duration for comparison in this study. This paper presents the relationships of H_{m0} and PSD and ship-based T_b at meter scales (footprint at 89 GHz at 55°: 6.36 m²; at 37 GHz: 6.62 m²) at 0.81 cm (37 GHz) and 0.34 cm (89 GHz) wavelengths.

We have used a C-band fully polarimetric scatterometer (ProSensing Inc., Amherst, MA, USA) (Table 1) installed on the port side of the *Amundsen* at a height of 7.6 m ASL

to collect backscatter signatures coincident to ocean buoy data over short (<0.5 hour) periods on 1, 9, and 26 of July. We collected backscatter and phase data at all four linear transmit/receive polarization combinations (HH, HV, VH, and VV) over the 20°–60° incidence angle range at 10° spacing and across a 60° azimuth centered perpendicular to the *Amundsen*. At 7.6 m height, and with the scatterometer positioned at a fixed azimuth and 45° incidence angle, its estimated footprint was 1.1 m². A single scan comprised several resolution cells over several meters by extending the azimuth to a 60° range, resulting in multiple statistically independent samples of the sea surface at each incidence angle. The use of a wide azimuth also increased the number of radar looks and reduced fading, though the resulting experimental dataset does not consider the wave direction relative to the scanning scatterometer. Isleifson et al. [32] and Geldsetzer et al. [33] have described the instrument calibration, noise levels, setup, and data limitations.

We placed a limit of 3 dB of signal-to-noise ratio on backscatter for analysis of scatterometer data, resulting in an upper incidence angle limit of 40° for scans taken during calm conditions. This limit extends to all samples to enable the intercomparison of all backscatter irrespective of sea state. The average covariance matrix, from which we derive HH, HV, and VV backscatter, as well as γ_{co} and γ_{cross}, using backscatter amplitudes, represents the scan data. We obtained the following polarimetric coherence parameters: the copolarized correlation coefficient (ρ_{VVHH}); the crosspolarized correlation coefficient (ρ_{HHVH}); and the coherence of right and left circular transmit/receive polarizations (ρ_{RRLL}) using the following formulae [34–36]:

$$\rho_{\text{VVHH}} = \frac{\langle |S_{\text{VV}} S_{\text{HH}}^*| \rangle}{\sqrt{\langle |S_{\text{VV}}|^2 \rangle \langle |S_{\text{HH}}|^2 \rangle}}, \tag{1}$$

$$\rho_{\text{HHVH}} = \frac{\langle |S_{\text{HH}} S_{\text{VH}}^*| \rangle}{\sqrt{\langle |S_{\text{HH}}|^2 \rangle \langle |S_{\text{VH}}|^2 \rangle}}, \tag{2}$$
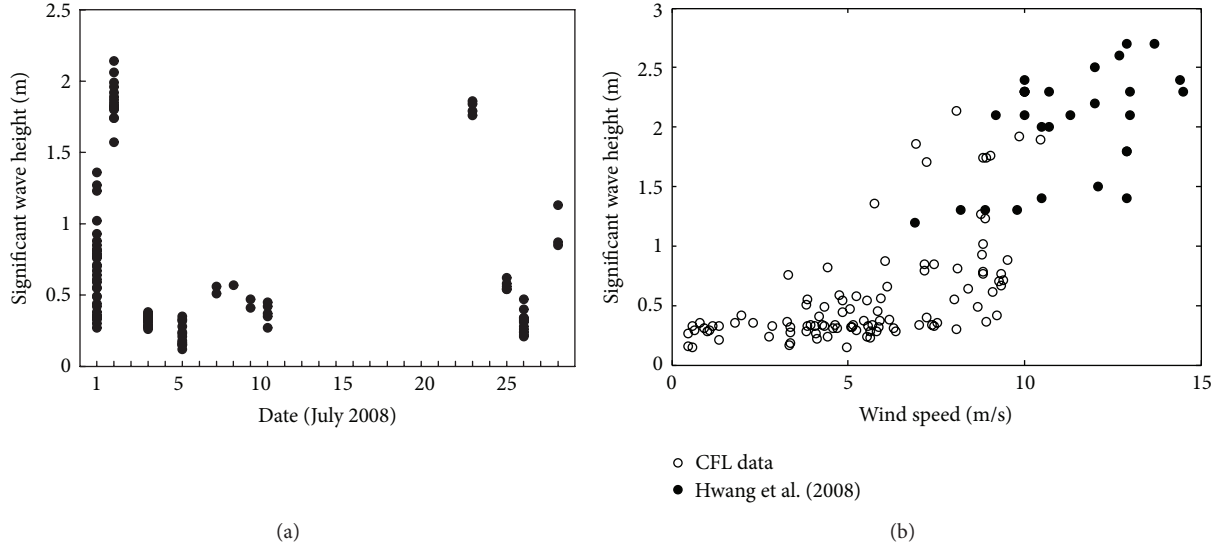
(a)

○ CFL data
● Hwang et al. (2008)

(b)

FIGURE 2: (a) Significant wave height (H_{m0}) observed from July 1 to 28, 2008 (total number of samples = 103). Multiple measurements on a day fall on the same vertical line. (b) H_{m0} is plotted versus wind speed and compared with data (total number of samples = 29) from Hwang et al. [40].

$$\rho_{RRLL} = \frac{\langle |S_{HH} - S_{VV}|^2 \rangle - 4 \langle |S_{HV}|^2 \rangle}{\langle |S_{HH} - S_{VV}|^2 \rangle + 4 \langle |S_{HV}|^2 \rangle}, \qquad (3)$$

$$\gamma_{co} = \frac{S_{VV}}{S_{HH}}, \qquad \gamma_{cross} = \frac{S_{HV}}{S_{HH}}, \qquad (4)$$

where S is the complex scattering matrix and an asterisk (*) represents the complex conjugate. The brackets $\langle \cdot \rangle$ represent ensemble averages of the observed data. Polarimetric coherences and polarization ratios have demonstrated utility in reducing the ambiguities caused by the nonlinearity between system response and target properties [37]. Further details on the derivation of ρ_{RRLL}, a parameter shown to be sensitive to surface roughness, are available in [38, 39].

3. Results and Discussion

3.1. Ocean Surface Wave Conditions. The data primarily represent wave breaking and energy dissipation of waves depending on the prevailing wind conditions. From the measured buoy data, H_{m0} ranged between 12 and 214 cm (sea state on Beaufort scale 0–5) compared to those by Hwang et al. [40] who reported a range of 120–270 cm in the Atlantic Ocean (Figure 2). Observed wave numbers ranged between 0.083 and 0.729 rad/m, and the wind speeds ranged between 0.5 and 10.5 m/s compared to wind speed range of 7.0–14.5 m/s given by Hwang et al. [40]. The wave steepness, in this paper, ranged between 0.011 and 0.050, which corresponded with the wavelength ranging between 8.61 and 75.56 m. The wave periods of wind-generated waves addressed in this paper lie between 2.4 and 7.0 sec. We did not observe swells (wave period > 10 sec [41]) during the field program. The observed relationship between the nondimensional form of energy,
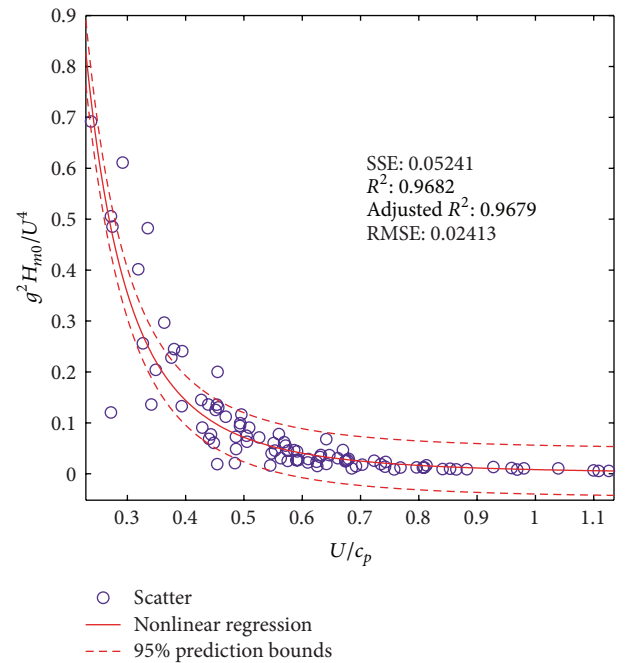

○ Scatter
— Nonlinear regression
- - - 95% prediction bounds

FIGURE 3: The plot shows the wind-generated wave condition in the experiment. Nonlinear model $y = ax^b$ between nondimensional wave energy (y-axis) and wave age (x-axis) indicates wind-induced wave development. SSE is the sum of squared error of the fit.

$g^2 H_{m0}/U^4$ (where g is gravitational acceleration), and wave age, U/c_p (where c_p is wave phase speed), as initially proposed by Kitaigorodskii [42] and further developed by Donelan et al. [43], supports the wind-generated wave growth in the data (Figure 3). The RMS error in the fitted curve is 0.024; the

TABLE 2: Scatterometer measurement dates and times, sampling durations, near and far range numbers of independent samples (n_{ind}) of the sea surface, with coincident wind speed, wave roughness parameters, significant wave height (H_{m0}), and power spectral density (PSD).

Date (2008)	Time (UTC)	Duration (minutes)	Radar n_{ind} (near)	Radar n_{ind} (far)	Wind speed (m/s)	Wave PSD (m²/Hz)	Wave H_{m0} (cm)
July 1	18:37	14	44	122	7.4	4.3154	136
July 9	16:57	17	44	122	5.8	0.2787	66
July 26	17:49	24	66	198	3.9	0.4617	47

Note. UTC: Universal Time Coordinated.

TABLE 3: Correlation matrix (Pearson's r) of observed variables. The number of samples of each variable is 111.

	T_b89H	T_b89V	T_b37H	T_b37V	H_{m0}	PSD	T_w	U
T_b89H	1							
T_b89V	**0.93**	1						
T_b37H	**0.97**	**0.88**	1					
T_b37V	**0.85**	**0.91**	**0.87**	1				
H_{m0}	**0.80**	**0.72**	**0.78**	0.55	1			
PSD	**0.71**	**0.64**	**0.70**	0.52	**0.92**	1		
T_w	0.25	0.44	0.16	0.21	0.25	0.20	1	
U	0.06	−0.02	0.09	−0.08	0.24	0.21	0.09	1

Note: T_b89H: brightness temperature at 89 GHz H-polarization (K).
T_b89V: brightness temperature at 89 GHz V-polarization (K).
T_b37H: brightness temperature at 37 GHz H-polarization (K).
T_b37V: brightness temperature at 37 GHz V-polarization (K).
H_{m0}: significant wave height (cm).
PSD: wave power spectral density (m²/Hz).
T_w: water temperature (°C).
U: wind speed (m/s).
Numerals in **bold** represent statistically significant correlation at the 95% confidence level.

coefficient of determination, $R^2 = 0.97$; and sum of residual errors, SSE = 0.052. The observed empirical relationship is

$$\frac{g^2 H_{m0}}{U^4} = 0.00817 \left(\frac{U}{c_p}\right)^{-3.132}. \tag{5}$$

Table 2 shows wave roughness parameters H_{m0} and PSD, coincident to scatterometer acquisitions on July 1, 9, and 26, 2008, along with U. While the scatterometer took eight minutes to complete one scan, wave height and PSD data were logged at 30-minute intervals. Table 2 also provides a summary of independent scatterometer samples acquired at 20° and 40° incidence angles, the near and far ranges examined in this study. Figure 4 shows the wave spectra from the same dates relative to the analytical Pierson-Moskowitz (P-M), Bretschneider, and 3-parameter Gamma wave spectra. These wave spectra considered both capillary and gravity wave (wavelength > 1.74 cm) development. The observed spectra is in agreement with the modeled spectra for the H_{m0} case on July 9, with peak frequencies of ~0.2 Hz. The observed spectra agree more closely with the P-M model at wave frequency greater than 0.2 Hz for other H_{m0} cases. The H_{m0} cases also contain more observed wave energy in the low frequency part of the observed spectra, indicating the presence of longer waves. The low frequency (larger waves) part of the spectra is marginally modeled by the wave spectra models, likely because of insufficient number of statistical data points of long wavelength waves available to generate a spectrum that fits the analytical spectrum. Also, the data lacked the longer wavelength waves or swell observations. Therefore, we consider only the wave frequencies of 0.2 Hz and above in the present treatment. The high H_{m0} at low wind speeds indicates that the wave energy still retained in the ocean even after winds have subsided. This transition from calm to rough sea (and vice versa) depends on the rate of wave energy dissipation in the ocean (Figures 2(b) and 4). These observed wave conditions set the background for which we investigate the microwave signatures of ocean surface in the next section.

3.2. Comparison to Passive and Active Microwave Signatures.

Table 3 shows the linear associations between geophysical variables (H_{m0}, PSD, water temperature, and U) and T_b at 37 and 89 GHz as a correlation matrix. We observed a low probability value (P value < 0.05) for each combination of bolded variables given in Table 3, verifying statistical significance. Table 4 provides the regression coefficients for estimating the H_{m0} using T_b and Figure 5 shows pertinent regression relationships. Wind speed does not correlate with T_b; however, we observe that T_b at 37 GHz and 89 GHz shows significant correlation with the H_{m0} and the PSD of the waves and the correlation is stronger for H-polarization than V-polarization. Thus, the higher T_b H-polarization implies an indirect contribution of wind energy in inducing wave heights than V-polarization. We did not observe any linear relationships between water surface temperature and T_b. Besides this, several other external factors that alter the

TABLE 4: Regression coefficients for H_{m0} and T_b for various frequencies and polarizations. The fitted line is $T_b = a + bH_{m0}$. Each regression contained 124 samples. We observed statistically significant linear regression for each frequency and polarization, with good correlation of T_b at H-polarization of 89 GHz with H_{m0}.

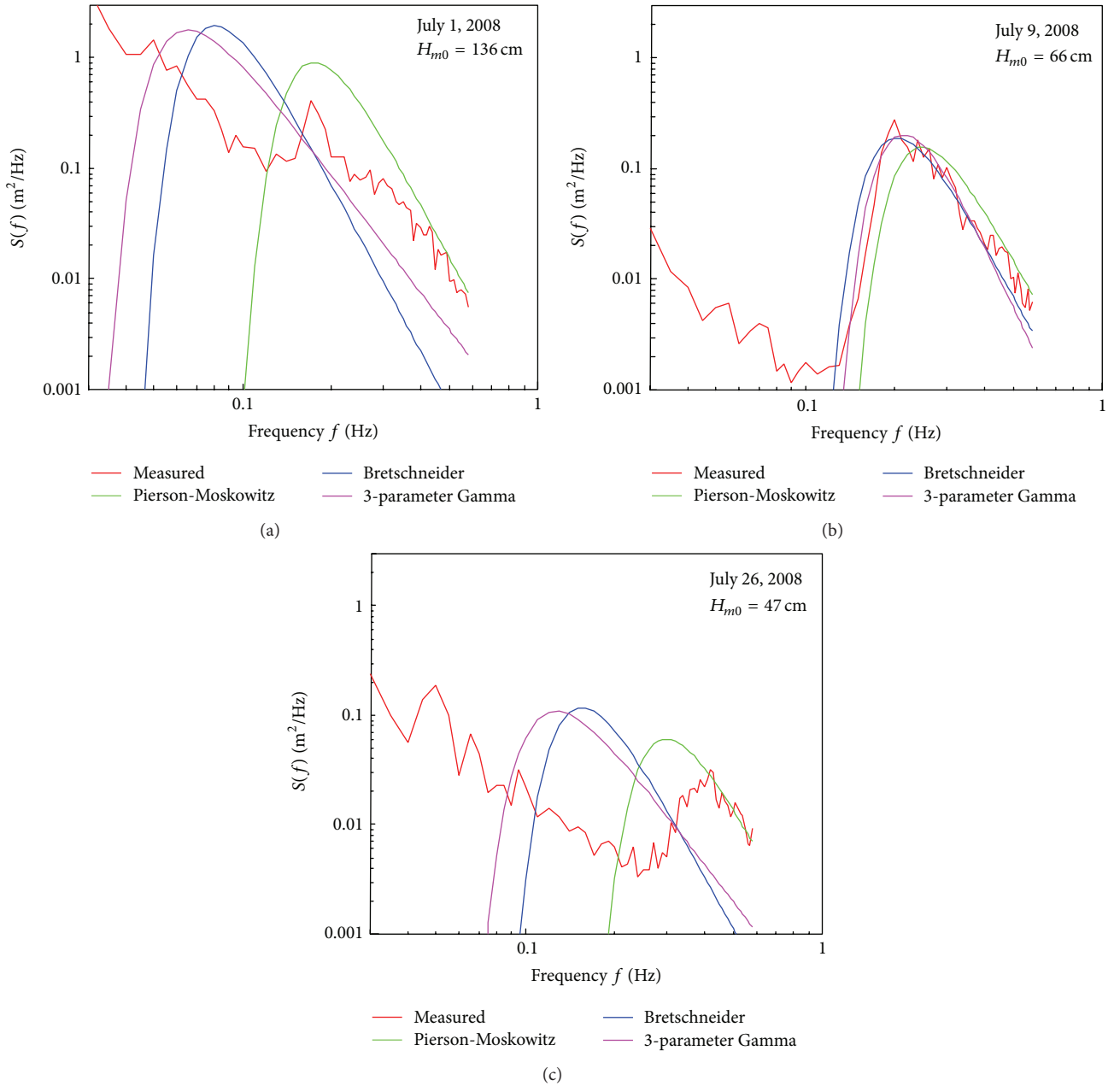|	a	b	P value (95% confidence interval)	Lower and upper bounds for b	Pearson's r
89H	173.98	0.15	<0.001	0.13, 0.18	0.74
89V	240.00	0.04	<0.001	0.03, 0.05	0.65
37H	120.60	0.10	<0.001	0.08, 0.12	0.74
37V	201.51	0.03	<0.001	0.02, 0.03	0.51

(a)

(b)

(c)

FIGURE 4: The wave spectra measured coincident to scatterometer on July 1, 9, and 26, 2008 with comparisons to analytical spectra. *Red*: measured; *green*: Pierson-Moskowitz; *blue*: Bretschneider; *magenta*: 3-parameter Gamma.
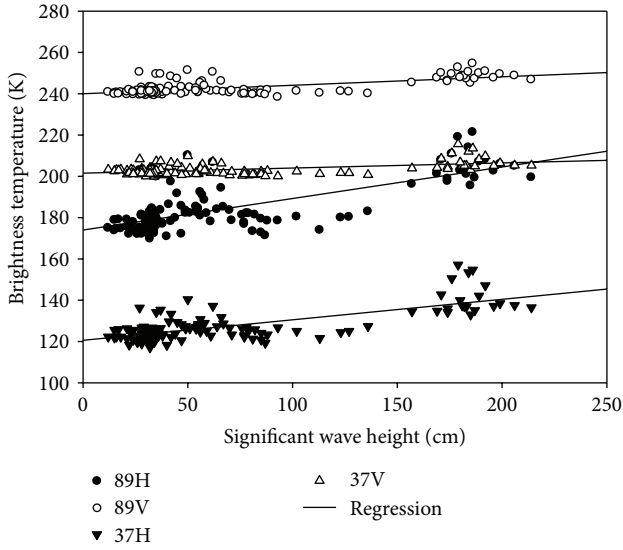
Figure 5: Relationship between brightness temperature (T_b) and H_{m0} at 37 and 89 GHz frequencies and horizontal (H) and vertical (V) polarizations.

passive microwave emission of the ocean surface affect the T_b.

Although the T_b depends on several other external factors (see Introduction), an increase in the surface area exposed to the sensor also contributes to a rise in T_b. Higher waves have a larger surface area, and the H-polarization especially detects the associated rise in T_b. The passive microwave frequencies used in the study are sensitive to the individual contributions of small-scale features; for example, sea spray and whitecaps. However, at the observed Beaufort scale 0–5, sea sprays are not significant; thus, we assume the contribution of spray to modifying the T_b as negligible. We observed an increase in H-polarization T_b at 37 and 89 GHz. This increase is consistent with the H-polarization observations by previous researchers. T_b increases with wind speed, foam, and whitecaps coverage at 8.36 and 19.34 GHz frequencies [9, 44] and between 13.4 and 37 GHz [45]. Other results illustrate a nonsignificant correlation between T_b and wind speed at V-polarizations of 6.6, 10.69, and 37 GHz frequencies [46]. In continuation of above studies, our results further confirm that the T_b at H-polarization is stronger than T_b at V-polarization at 37 and 89 GHz under rougher conditions.

Backscatter is compared to H_{m0} and considered in the context of surface roughness at the C-band scale. The inter-action of incident radar waves with the capillary waves (millimeter level), whose restoring force is the surface tension of the water, is not accounted for, as the waves of this size are not detectable by the Waverider buoy. We compared the buoy-measured gravity waves, whose restoring force is gravity, with the backscatter. Kudryavtsev [47] has described the relationship between gravity (demonstrated as wave height) and capillary (demonstrated as Bragg scattering) waves. Figures 6(a) and 6(b) show the VV and HV backscatter at incidence angles 20°, 30°, and 40° for the three radar-H_{m0} cases. The plots include backscatter intensities to provide insight into

the relative contributions of gravity and capillary waves. We observed a decrease in backscatter with the increasing incidence angle, as expected, over the sampled range. The highest intensities correspond to the highest H_{m0} on July 1, though the weakest intensities correspond to the intermediate H_{m0} on July 9. Stronger HH (not shown), HV, and VV backscatter at all incidence angles for the lowest H_{m0} on July 26, relative to July 9, points to the likelihood of a stronger coupling of the radar waves to capillary waves, implying that higher capillary waves interaction with microwaves results in higher backscatter even at intermediate H_{m0}.

Figures 7(a) and 7(b) show the γ_{co} and γ_{cross} for each of the analyzed incidence angles and roughness conditions. If we consider the roughness, interpreted using the HV and VV intensities in Figure 6, instead of the measured H_{m0}, the γ_{co} at 20° shows consistent behavior. The γ_{co} shows an inverse relation to the radar-interpreted roughness in a manner consistent with Bragg and Integral Equation Model (IEM) surface backscattering models [48]. The γ_{co} for given incidence angle and dielectric constant, according to Bragg and IEM theory, tends to zero (greater HH relative to VV) with increasing surface roughness provided that the surface roughness is greater than, or equal to the incident wavelength. The γ_{co} is independent of surface roughness for smooth surfaces with surface height very small relative to the incident wavelength [38]. The additional HH backscatter relative to VV is so strong for the roughest H_{m0} case on July 1 that the ratio at 20° becomes negative. For such a sea state, previous observations show greater HH backscatter sensitivity to the tilt modulation effect caused by larger waves on Bragg waves [23, 49], as well as wave breaking [50].

Our observations show correlation, which appears to be qualitatively proportionate, between γ_{co} and H_{m0} at 40° incidence angle; that is, H_{m0} and γ_{co} are much stronger on July 1 while July 9 and July 26 are similar. However, the results of Mouche et al. [24] show that one must consider azimuth angle (direction of waves relative to the radar look angle) at incidence angles larger than 25°. We have not considered it in the three cases evaluated in this study. In Figure 7(b), there is a significant increase in γ_{cross} as a function of incidence angle and a small diversity between sea states. At 40° incidence angle, there is an increase in the ratio of 2 dB between the smooth and rough H_{m0} cases, and the ratio shows correlation with the H_{m0}. This effect is most likely because of the combined loss of HV backscatter with the incidence angle, which is also evident in Figure 6, coupled with an increased sensitivity of VV backscatter to the sea state. The HV intensity values are very low at incidence angles of 40° and above, in the context of utilizing γ_{cross} from spaceborne SAR and one must consider it relative to the noise equivalent sigma zero of the utilized sensor at a particular incidence angle.

Figures 8(a)–8(c) provide polarimetric coherence parameters ρ_{HHVH}, ρ_{VVHH}, and ρ_{RRLL} at each of the incidence angles and roughness conditions. Figure 8(a) shows the ρ_{HHVH}, a measure of the correlation between complex HH and VH returns. There appears to be no relationship between ρ_{HHVH} and H_{m0} under the constraints imposed in this study. However, the ρ_{VVHH} in Figure 8(b) shows an inverse relationship between the magnitude of the coherence and H_{m0} at 20°
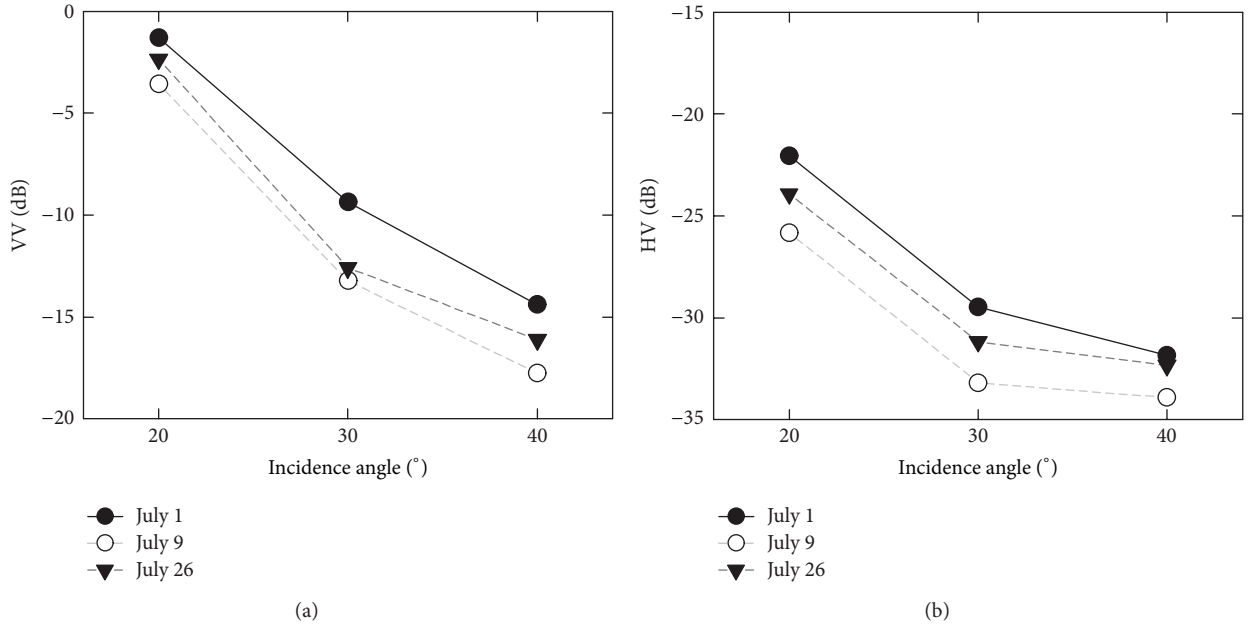
FIGURE 6: Incidence-angle-dependent (a) VV and (b) HV backscatter from wind-roughened open water on July 1 ($H_{m0} = 136$ cm), July 9 ($H_{m0} = 66$ cm), and July 26 ($H_{m0} = 47$ cm).
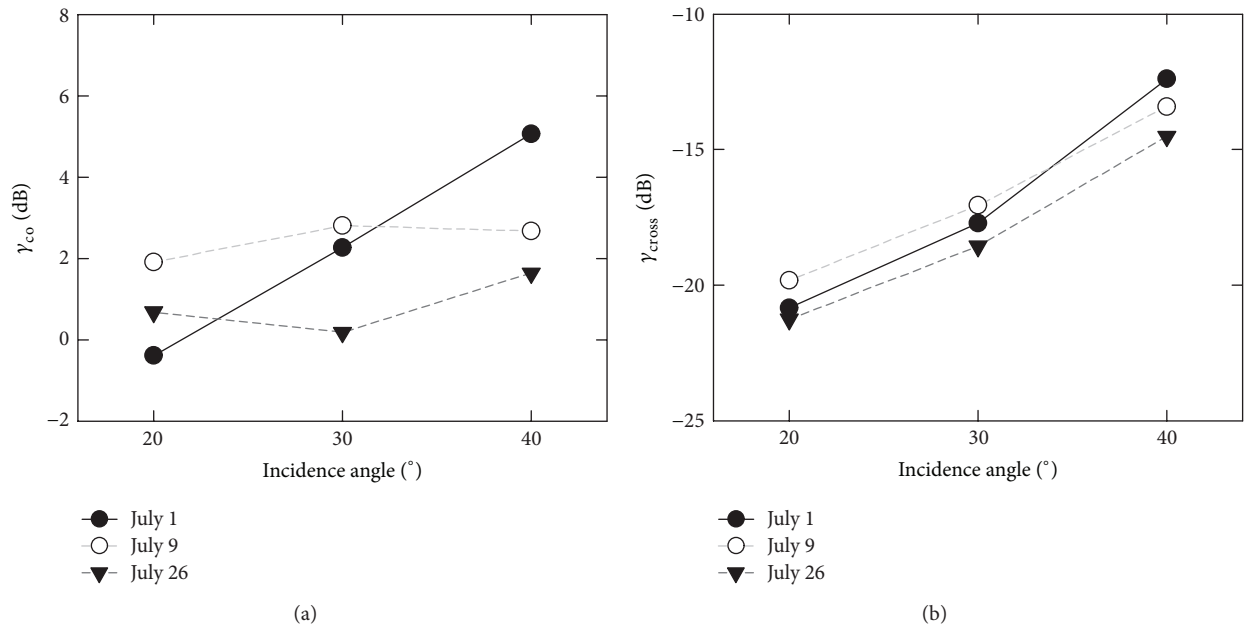

FIGURE 7: Incidence-angle-dependent ratios (a) γ_{co} and (b) γ_{cross} from wind-roughened open water on July 1 ($H_{m0} = 136$ cm), July 9 ($H_{m0} = 66$ cm), and July 26 ($H_{m0} = 47$ cm).

incidence angle. This is consistent with a depolarization of incident polarized radar energy induced by the rougher ocean waves. Beyond 20°, there is no discernible relationship between H_{m0} and ρ_{VVHH} that one can deduce based on expected scattering mechanisms. Similar magnitudes of the correlation coefficient are evident for sea states on July 9 and 26. The rough sea state on July 1 (also seen at 20°) suggests that this parameter has utility for discriminating higher

waves. One expects the parameter ρ_{RRLL} in Figure 8(c) to be decreasing with increasing surface roughness [34, 38, 51], though researchers developed it for terrestrial applications and did not verify for an ocean surface. At 20°, there is only a negligible decrease in ρ_{RRLL} associated with the highest H_{m0} case on July 1. The rougher sea state is linked with the highest ρ_{RRLL} at incidence angles greater than 20°. This is contrary to previous results over terrestrial surfaces. An
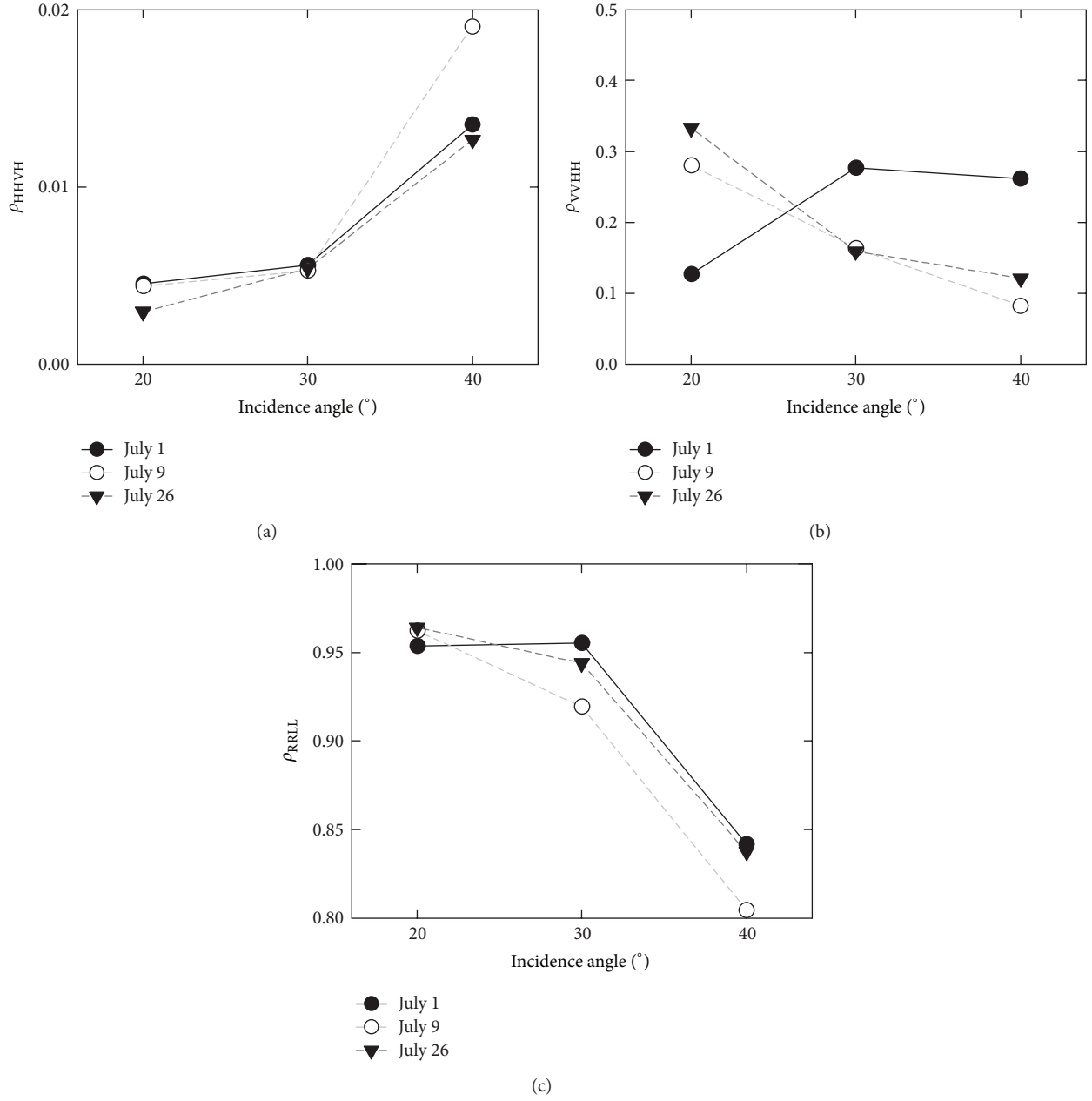
(a)

(b)

(c)

FIGURE 8: Incidence-angle-dependent polarimetric coherences (a) ρ_{HHVH} (b) ρ_{VVHH}, and (c) ρ_{RRLL} from wind-roughened open water on July 1 ($H_{m0} = 136$ cm), July 9 ($H_{m0} = 66$ cm), and July 26 ($H_{m0} = 47$ cm).

important consideration, however, is the scale of physical roughness, which is much greater for the ocean waves under investigation in this study. Furthermore, in a study of Jet Propulsion Laboratory (JPL) polarimetric scatterometer observations off the California coast at 13.4 GHz, Lee et al. [52] found an azimuthal dependency on the ρ_{RRLL}, but did not specify the incidence angle. The study of γ_{co} by Keller et al. [22] (at C-band) mentioned above shows that one must consider the azimuth effect above 25° for this coherence. The C-band radar observations in this study, particularly γ_{co}, results in Figure 7(b), and the coherence results in Figures 8(a)–8(c), further support the need to consider ambiguity

caused by the azimuth angle when considering the derivation of sea state from polarimetric radar data at incidence angles greater than 25°.

4. Conclusions

We presented, in this paper, passive microwave emission and polarimetric backscatter data coincident to wind and ocean buoy data at unique spatial and temporal scales relative to airborne and satellite remote sensing studies. A statistical analysis of coincident geophysical variables showed that the

T_b is more sensitive to H_{m0} than the wind speed at both H- and V-polarizations and that it shows stronger correlation with H_{m0} at H-polarization. The PSD and H_{m0} show significant correlation with the H-polarization of T_b at both of the passive microwave frequencies (better with 37 GHz because of longer wavelength) in this study. An assessment of C-band backscatter points to a dependency of HV and VV intensities on surface roughness, which is resonant to the radar frequency, but not captured by the Waverider buoy, as shown by greater backscatter intensities for the smoother H_{m0} (47 cm compared to 66 cm) at each of the observed incidence angles. γ_{co} and γ_{cross} at 40° are positively associated with H_{m0}, and γ_{co} particularly shows an increase that is proportional to H_{m0}.

The polarimetric coherence parameter ρ_{VVHH} at 20° also shows an inverse relationship with H_{m0} because of an expected decorrelation of complex returns with greater surface roughness. The ρ_{VVHH} also holds potential for discriminating rough ($H_{m0} = 136$ cm) from smooth ($H_{m0} \leq 66$ cm) sea states at 30° and 40°, based on an increase in the magnitude of ρ_{VVHH} with increasing H_{m0}. We did not observe a decrease in ρ_{RRLL} with increasing roughness, as expected for all incidence angles based on previous observations made over terrestrial surfaces. While the results presented here point to the utility of C-band satellite radar for deriving ocean surface physical roughness information without the need for wind speed or azimuth angle information at incidence angles less than approximately 25°, importantly they provide a stimulus for further investigations including the azimuth angle for observations above approximately 25°. With an increasing spatial and temporal coverage of open water in the Arctic, it will be important to develop robust satellite retrieval algorithms which examine both gas and energy exchange across the AO interface and into the marginal ice zones (MIZ) of the Arctic.

Conflict of Interests

The authors declare that there is no conflict of interests regarding the publication of this paper.

Acknowledgments

References

[1] D. G. Barber and J. M. Hanesiak, "Meteorological forcing of sea ice concentrations in the southern Beaufort Sea over the period 1979 to 2000," *Journal of Geophysical Research C*, vol. 109, no. 6, Article ID C06014, 2004.

[2] J. V. Lukovich and D. G. Barber, "On sea ice concentration anomaly coherence in the southern Beaufort Sea," *Geophysical Research Letters*, vol. 32, no. 10, Article ID L10705, 2005.

[3] E. C. Carmack and R. W. Macdonald, "Oceanography of the Canadian shelf of the Beaufort Sea: a setting for marine life," *Arctic*, vol. 55, no. 1, pp. 29–45, 2002.

[4] W. O. Smith Jr. and D. G. Barber, Eds., *Polynyas: Windows to the World*, Elsevier, Amsterdam, The Netherlands, 2007.

[5] H. He and D. Chen, "Effects of surface wave breaking on the oceanic boundary layer," *Geophysical Research Letters*, vol. 38, no. 7, Article ID L07604, 2011.

[6] I. N. Esau, "Amplification of turbulent exchange over wide Arctic leads: large-eddy simulation study," *Journal of Geophysical Research D*, vol. 112, no. 8, Article ID D08109, 2007.

[7] K. St. Germain, G. A. Poe, and P. W. Gaiser, "Polarimetric emission model of the sea at microwave frequencies and comparison with measurements," *Progress in Electromagnetics Research*, vol. 37, pp. 1–30, 2002.

[8] S. H. Yueh, "Modeling of wind direction signals in polarimetric sea surface brightness temperatures," *IEEE Transactions on Geoscience and Remote Sensing*, vol. 35, no. 6, pp. 1400–1418, 1997.

[9] J. P. Hollinger, "Passive microwave measurements of sea surface roughness," *IEEE Transactions on Geoscience Electronics*, vol. 9, no. 3, pp. 165–169, 1971.

[10] F. T. Ulaby, R. K. Moore, and A. K. Fung, *Microwave Remote Sensing: Active and Passive—Volume 3: Scattering and Emission Theory, Advanced Systems and Applications*, Artech House, Dedham, Mass, USA, 1986.

[11] Y. A. Kravtsov and A. N. Churyumov, "Contribution of steep irregularities to the radio-brightness temperature of the ocean," *Radiophysics and Quantum Electronics*, vol. 43, no. 3, pp. 196–201, 2000.

[12] E. C. Monahan and I. G. O'Muircheartaigh, "Whitecaps and the passive remote sensing of the ocean surface," *International Journal of Remote Sensing*, vol. 7, no. 5, pp. 627–642, 1986.

[13] A. E. Strong, "Mapping sea-surface roughness using microwave radiometry," *Journal of Geophysical Research*, vol. 76, no. 36, pp. 8641–8648, 1971.

[14] W. Nordberg, J. Conaway, D. B. Ross, and T. Wilheit, "Measurements of microwave emission from a foam-covered, wind-driven sea," *Journal of Atmospheric Sciences*, vol. 28, no. 3, pp. 429–435, 1971.

[15] O. M. Phillips, "Radar returns from the sea surface—Bragg scattering and breaking waves," *Journal of Physical Oceanography*, vol. 18, no. 8, pp. 1065–1074, 1988.

[16] D. Vandemark, B. Chapron, J. Sun, G. H. Crescenti, and H. C. Graber, "Ocean wave slope observations using radar backscatter and laser altimeters," *Journal of Physical Oceanography*, vol. 34, no. 12, pp. 2825–2842, 2004.

[17] H. Hersbach, "Comparison of C-Band scatterometer CMOD5.N equivalent neutral winds with ECMWF," *Journal of Atmospheric and Oceanic Technology*, vol. 27, no. 4, pp. 721–736, 2010.

[18] H. Hersbach, A. Stoffelen, and S. de Haan, "An improved C-band scatterometer ocean geophysical model function: CMOD5," *Journal of Geophysical Research C*, vol. 112, no. 3, Article ID C03006, 2007.

[19] A. S. Komarov, V. Zabeline, and D. G. Barber, "Ocean surface wind speed retrieval from C-band SAR images without input of wind direction," *IEEE Transactions on Geoscience and Remote Sensing*, vol. 52, no. 2, pp. 980–990, 2014.

[20] A. Stoffelen and D. Anderson, "Scatterometer data interpretation: measurement space and inversion," *Journal of Atmospheric and Oceanic Technology*, vol. 14, no. 6, pp. 1298–1313, 1997.

[21] W. L. Jones and L. C. Schroeder, "Radar backscatter from the ocean: dependence on surface friction velocity," *Boundary-Layer Meteorology*, vol. 13, no. 1–4, pp. 133–149, 1978.

[22] W. C. Keller, V. Wismann, and W. Alpers, "Tower-based measurements of the ocean C band radar backscattering cross section," *Journal of Geophysical Research*, vol. 94, no. 1, pp. 924–930, 1989.

[23] D. R. Thompson, T. M. Elfouhaily, and B. Chapron, "Polarization ratio for microwave backscattering from the ocean surface at low to moderate incidence angles," in *Proceedings of the IEEE International Geoscience and Remote Sensing Symposium (IGARSS '98)*, pp. 1671–1673, Seattle, Wash, USA, July 1998.

[24] A. A. Mouche, D. Hauser, J. Daloze, and C. Guérin, "Dual-polarization measurements at C-band over the ocean: results from airborne radar observations and comparison with ENVISAT ASAR data," *IEEE Transactions on Geoscience and Remote Sensing*, vol. 43, no. 4, pp. 753–769, 2005.

[25] V. Kudryavtsev, D. Hauser, G. Caudal, and B. Chapron, "A semiempirical model of the normalized radar cross-section of the sea surface 1. Background model," *Journal of Geophysical Research C*, vol. 108, no. 3, pp. FET 2-1–FET 2-24, 2003.

[26] V. Kudryavtsev, D. Hauser, G. Caudal, and B. Chapron, "A semiempirical model of the normalized radar cross section of the sea surface, 2. Radar modulation transfer function," *Journal of Geophysical Research C*, vol. 108, no. 3, pp. FET 3-1–FET 3-16, 2003.

[27] O. M. Phillips, "Spectral and statistical properties of the equilibrium range in the wind-generated gravity waves," *Journal of Fluid Mechanics*, vol. 156, pp. 505–531, 1985.

[28] G. R. Valenzuela, "Theories for the interaction of electromagnetic and oceanic waves—a review," *Boundary-Layer Meteorology*, vol. 13, no. 1–4, pp. 61–85, 1978.

[29] D. G. Barber, M. G. Asplin, Y. Gratton et al., "The international polar year (IPY) circumpolar flaw lead (CFL) system study: overview and the physical system," *Atmosphere-Ocean*, vol. 48, no. 4, pp. 225–243, 2010.

[30] K. Hunkins, "Waves on the Arctic Ocean," *Journal of Geophysical Research*, vol. 67, no. 6, pp. 2477–2489, 1962.

[31] L. D. Farmer, D. T. Eppler, and A. W. Lohanick, "Converting digital passive microwave radiances to Kelvin units of brightness temperatures," Technical Note 427, Naval Ocean Research and Development Activity (NORDA), Bay St. Louis, Miss, USA, 1990.

[32] D. Isleifson, B. Hwang, D. G. Barber, R. K. Scharien, and L. Shafai, "C-band polarimetric backscattering signatures of newly formed sea ice during fall freeze-up," *IEEE Transactions on Geoscience and Remote Sensing*, vol. 48, no. 8, pp. 3256–3267, 2010.

[33] T. Geldsetzer, J. B. Mead, J. J. Yackel, R. K. Scharien, and S. E. L. Howell, "Surface-based polarimetric C-band scatterometer for field measurements of sea ice," *IEEE Transactions on Geoscience and Remote Sensing*, vol. 45, no. 11, pp. 3405–3416, 2007.

[34] M. Gupta, R. K. Scharien, and D. G. Barber, "C-band polarimetric coherences and ratios for discriminating sea ice roughness," *International Journal of Oceanography*, vol. 2013, Article ID 567182, 13 pages, 2013.

[35] J.-S. Lee, D. L. Schuler, and T. L. Ainsworth, "Polarimetric SAR data compensation for terrain azimuth slope variation," *IEEE Transactions on Geoscience and Remote Sensing*, vol. 38, no. 5, pp. 2153–2163, 2000.

[36] D. L. Schuler, J.-S. Lee, D. Kasilingam, and G. Nesti, "Surface roughness and slope measurements using polarimetric SAR data," *IEEE Transactions on Geoscience and Remote Sensing*, vol. 40, no. 3, pp. 687–698, 2002.

[37] H. J. Eom and W.-M. Boerner, "Statistical properties of the phase difference between two orthogonally polarized SAR signals," *IEEE Transactions on Geoscience and Remote Sensing*, vol. 29, no. 1, pp. 182–184, 1991.

[38] I. Hajnsek, E. Pottier, and S. R. Cloude, "Inversion of surface parameters from polarimetric SAR," *IEEE Transactions on Geoscience and Remote Sensing*, vol. 41, no. 4, pp. 727–744, 2003.

[39] F. Mattia, T. L. Toan, J.-C. Souyris et al., "The effect of surface roughness on multifrequency polarimetric sar data," *IEEE Transactions on Geoscience and Remote Sensing*, vol. 35, no. 4, pp. 954–966, 1997.

[40] P. A. Hwang, M. A. Sletten, and J. V. Toporkov, "Analysis of radar sea return for breaking wave investigation," *Journal of Geophysical Research C*, vol. 113, no. 2, Article ID C02003, 2008.

[41] N. C. Wells, *The Atmosphere and Ocean*, John Wiley & Sons, Oxford, UK, 2012.

[42] S. A. Kitaigorodskii, "Applications of the theory of similarity to the analysis of wind-generated wave motion as a stochastic process," *Bulletin of the Academy of Sciences, USSR Geophysics Series*, vol. 1, pp. 105–117, 1962.

[43] M. Donelan, M. Skafel, H. Graber, P. Liu, D. Schwab, and S. Venkatesh, "On the growth rate of wind-generated waves," *Atmosphere-Ocean*, vol. 30, no. 3, pp. 457–478, 1992.

[44] J. P. Hollinger, "Passive microwave measurements of the sea surface," *Journal of Geophysical Research*, vol. 75, no. 27, pp. 5209–5213, 1970.

[45] A. Stogryn, "The emissivity of sea foam at microwave frequencies," *Journal of Geophysical Research*, vol. 77, no. 9, pp. 1658–1666, 1972.

[46] P. C. Pandey and R. K. Kakar, "An empirical microwave emissivity model for a foam-covered sea," *IEEE Journal of Oceanic Engineering*, vol. 7, no. 3, pp. 135–140, 1982.

[47] V. N. Kudryavtsev, "Physical model of the spectrum of capillary-gravity waves," *Physical Oceanography*, vol. 8, no. 2, pp. 69–80, 1997.

[48] A. K. Fung and K. S. Chen, *Microwave Scattering and Emission Models for Users*, Artech House, Norwood, Mass, USA, 2010.

[49] D. B. Trizna and D. J. Carlson, "Studies of dual polarized low grazing angle radar sea scatter in nearshore regions," *IEEE Transactions on Geoscience and Remote Sensing*, vol. 34, no. 3, pp. 747–757, 1996.

[50] H. Johnsen, G. Engen, and G. Guitton, "Sea-surface polarization ratio from envisat ASAR AP data," *IEEE Transactions on Geoscience and Remote Sensing*, vol. 46, no. 11, pp. 3637–3646, 2008.

[51] R. Touzi, W. M. Boerner, J. S. Lee, and E. Lueneburg, "A review of polarimetry in the context of synthetic aperture radar: concepts and information extraction," *Canadian Journal of Remote Sensing*, vol. 30, no. 3, pp. 380–407, 2004.

[52] J.-S. Lee, S. H. Yueh, and D. L. Schuler, "Polarimetric analysis of scatterometer data for ocean surface wind measurement," in *Proceedings of the IEEE International Geoscience and Remote Sensing Symposium (IGARSS '04)*, vol. 1, pp. 20–24, Anchorage, Alaska, USA, September 2004.

Journal of
Geochemistry

Scientifica

International Journal of
Ecology

The Scientific
World Journal

Journal of
Mining

Journal of
Earthquakes

Paleontology Journal

Journal of
Petroleum Engineering

International Journal of
Geophysics

Hindawi

Submit your manuscripts at
http://www.hindawi.com

Advances in
Meteorology

Journal of
Climatology

Advances in
Geology

Advances in
Oceanography

International Journal of
Oceanography

International Journal of
Mineralogy

Journal of
Geological Research

International Journal of
Atmospheric Sciences

Applied &
Environmental
Soil Science

Journal of
Computational
Environmental Sciences